

Emergence of a Fermi-surface in the current-driven Hidden state of 1T-TaS₂

Yuval Nitzav,¹ Roni Gofman,¹ Ilay Mangel,¹ Abigail Dishi,¹ Nitzan Ragoler,¹ Sajilesh K.P.,¹ Yaron Jarach,¹ Alex Louat,² Matthew D. Watson,² Cephise Cacho,² Irena Feldman,¹ and Amit Kanigel¹

¹*Physics Department, Technion-Israel Institute of Technology, Haifa 32000, Israel.*

²*Diamond Light Source, Harwell Science and Innovation Campus, Didcot, OX11 0DE, UK*

(Dated: September 2023)

We investigate the nature of the metallic metastable state in 1T-TaS₂. Using microARPES, we measure the spatially-dependent modifications of the electronic structure of the sample following a short current pulse. We observe that, in some regions of the sample, a Fermi surface emerges, while other regions remain gapped. A detailed study of the band structure in these different regions suggests that the metallic parts are in a state similar to the nearly commensurate charge density wave (NC-CDW) state, where the gaps are suppressed and a band crosses the Fermi level. Furthermore, we find that the metallic and insulating regions of the sample exhibit different dispersions normal to the planes. This observation is consistent with a scenario in which the current pulse breaks the star-of-David dimers present in the commensurate charge density wave (C-CDW) state.

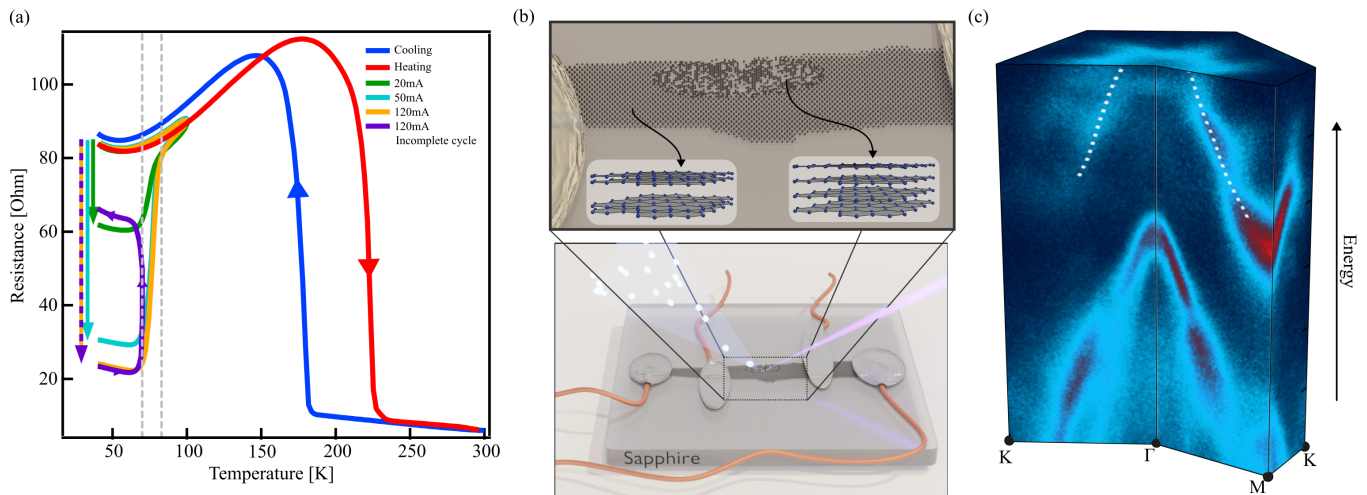


FIG. 1. **The hidden meta-stable state in 1T-TaS₂.** (a) Resistance as a function of temperature for a typical sample used in the ARPES experiment. The blue and red curves represent the sample resistance during cooling and heating, respectively, without any perturbation. The green, cyan, and orange curves illustrate the reduction in resistance with the application of progressively larger current pulses. The purple curve shows an incomplete recovery to the "normal" state after the application of a 120mA pulse. (b) Schematic illustration of the microARPES experiment. A thin 1T-TaS₂ sample is fixed to a sapphire substrate using Ag-epoxy. Four contacts are used to apply current and measure the voltage across the sample. A micron-sized beam spot is employed to scan the electronic spectrum of the device. In the hidden state, the sample is phase-separated into insulating and metallic areas. The out-of-plane dispersion indicates that the unit cell in the insulating regions is twice the size of the unit cell in the metallic regions. (c) ARPES data from the metallic part along high symmetry lines. Following the current pulse, a Fermi surface emerges in parts of the sample. The dispersion of the NC-CDW at 300K is indicated by the dotted white line.

I. INTRODUCTION

A metastable state refers to a state of a system that is not in its lowest energy state, but persists for a relatively long time before eventually transitioning to a more stable state. Some metastable states can be reached thermally (e.g., by quenching the system from an elevated temperature) [1, 2], while others are 'hidden' and can only be accessed through non-thermal perturbations [3–6].

One such hidden phase is the metallic state induced at low temperatures in 1T-TaS₂ by various stimuli, including a short light pulse [7], charge transfer [8], or a short electric current pulse [9]. Regardless of the perturbation method, the hidden state exhibits a similar critical temperature [10] and relaxation time scales [11]. Following the short pulse, the resistance of the samples is reduced by up to several orders of magnitude. This hidden metallic state has been shown to persist for hours and is fully reversible either when the sample is heated above a certain temperature [11] or subjected to an erasing pulse [7].

Due to the fast and controllable nature of the transition to the hidden state [12], it has been suggested for various applications, including programmable light manipulation [13] and charge configuration memory (CCM) devices [9, 10, 14, 15].

The origin of the insulating ground state of 1T-TaS₂ is still not fully understood. The electronic-structure is governed by a charge density wave (CDW) instability [16, 17]. The main motif of the CDW is a rearrangement of every 13 Ta atoms in a star-of-David cluster where 12 Ta atoms are displaced towards the middle 13th atom. Below 352K domains of star-of-David super-cells start to form. The domains are separated by regions with no CDW and form an hexagonal lattice which is nearly commensurate (NC) with the atomic lattice [18–20]. Below 183K all the star-of-David domains merge to create a commensurate CDW (C-CDW) state. The C-CDW vectors are rotated by ± 13.9 degrees from the atomic lattice vectors and form a new $\sqrt{13} \times \sqrt{13}$ sized unit cell. The orientation of the CDW vectors breaks mirror symmetry, and gives rise to two degenerate configurations (see Fig.4) with a distinct chirality. The sample's chirality is established during the formation of the CDW domains in the NC-CDW phase and persists into the C-CDW state [21]. It has been found that in the C-CDW state, these chiral domains can extend to millimeter-scale sizes [22].

The phase transition from NC-CDW to C-CDW is marked by an abrupt increase in resistivity, followed by strong insulating behavior at lower temperatures. In the C-CDW state, the valence band splits into seven narrow bands, six of which are fully occupied, while the topmost band is half-filled. The presence of unpaired electrons suggests that

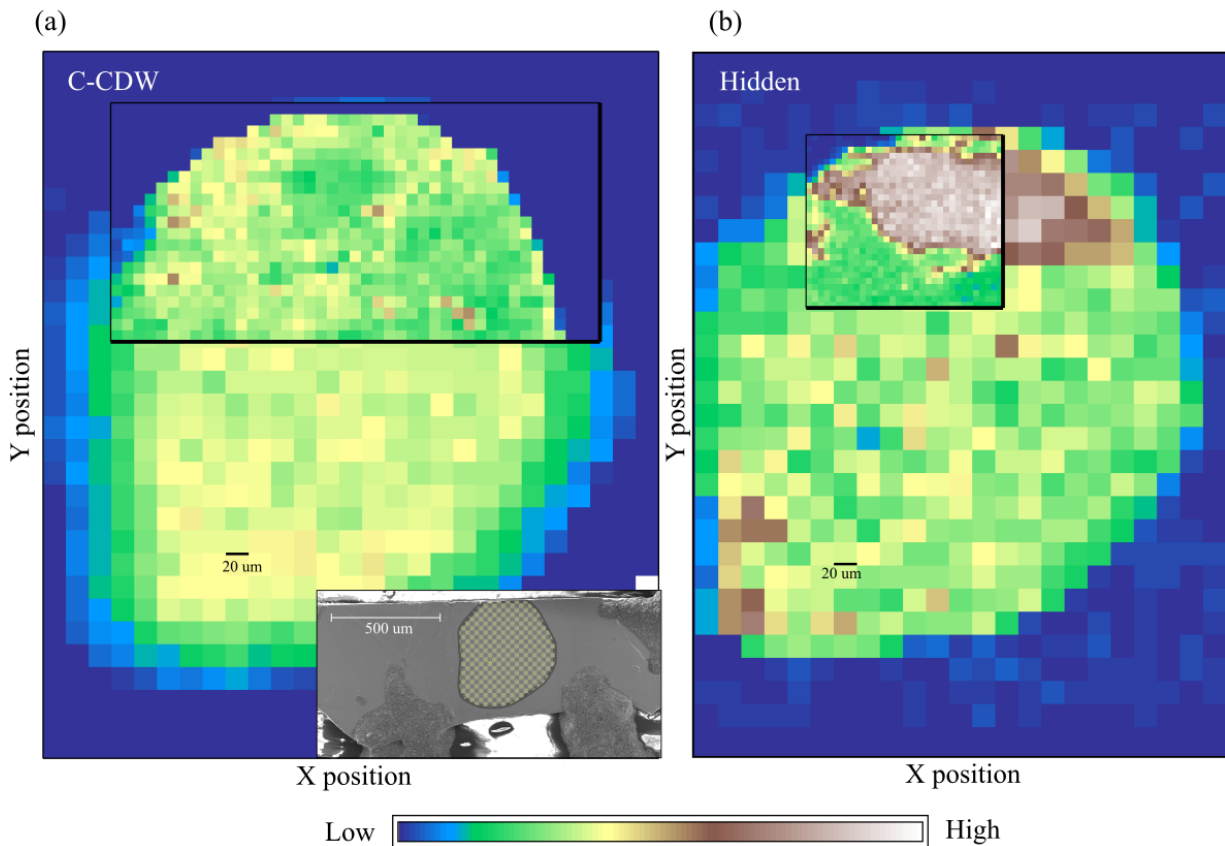


FIG. 2. **Maps of the spectral weight at the Fermi level.** microARPES maps were measured with a spot size of 5 microns at 40K. The step size was set to 20 microns, and reduced in the area marked by a solid black line to 10 microns in (a) and 5 microns in (b). The color map represents the integrated ARPES intensity at the Fermi level. In (a), we show the sample in the C-CDW state. The sample was warmed and then cooled back down after being measured in the hidden state. The entire scan shows low intensity, indicating a gapped state. The inset is a SEM image showing the sample with Ag-epoxy contacts, with the cleaved area marked on the image. In (b), we show a spatial scan after a 190mA current pulse. High-intensity regions can be seen. In these areas, the gap is closed, and we observe a metallic Fermi-Dirac edge.

C-CDW alone cannot fully explain the observed insulating state [23, 24].

It has been proposed that the narrow half-filled band in $1T\text{-TaS}_2$ undergoes a Mott transition to an insulating state[25, 26]. In recent years, it has become evident that the out-of-plane stacking of star-of-David clusters plays a significant role in determining the electronic properties of $1T\text{-TaS}_2$ [27, 28]. Evidence for out-of-plane dimerization is observed during the transition to the C-CDW state[29], resulting in an even number of electrons per unit cell and leading to insulating behavior[30]. Understanding the nature of the metallic hidden state may provide insights into the origin of the insulating ground state.

In this paper, we use spatially resolved ARPES to track the evolution of the electronic structure of $1T\text{-TaS}_2$ after a short current pulse. Our main results are summarized in Fig. 1. Following a short current pulse, the resistance of the sample at low temperatures decreases by a factor of about four (Fig. 1a). In this state, we observe a non-uniform electronic structure, with different parts of the sample exhibiting distinct behaviors (Fig. 1b). Most of the sample remains in the C-CDW state, characterized by a full gap and a clear band folding due to the CDW both in-plane and out-of-plane. However, other regions, which contribute to the enhanced conductance in the hidden state, display a much weaker CDW effect and have a clear Fermi surface (Fig. 1c). The ARPES spectrum in these parts has some similarities with the NC-CDW spectrum although STM measurements find a completely different domain morphology in the two states [31].

II. RESULTS AND DISCUSSION

Narrow bridges were cut from a single crystal of 1T-TaS₂ and four contacts were made using Ag epoxy (for more details about the sample preparation see the Methods section). In Fig. 1(a), we present the resistance as a function of temperature for a typical bridge. An abrupt change in resistance is observed when cooling into the C-CDW state at approximately 180K (blue line) and when warming back up at around 220K.

At a temperature of 40 K, a DC current pulse was applied, drastically lowering the sample's resistance. This low resistance is maintained as long as the temperature remains below 70 K, which is consistent with the transition temperature observed when a short light pulse was used to drive the transition [11].

As higher current pulses are applied, the sample's resistance decreases further, eventually saturating at around 140-190 mA for our typical sample dimensions. Upon warming, the resistance returns to its initial value. If the sample is cooled before a complete transition back to the C-CDW phase, it becomes locked in an intermediate state (see the purple line in Fig. 1a).

In Fig. 2 we show maps of the spectral weight at the Fermi-level over the entire cleaved area in the C-CDW state (Fig. 2(a)) and in the hidden state (2(b)). The color map represents the momentum-integrated intensity of the microARPES spectra at the Fermi-level. The spatial resolution is set by the spot size which is about 5 microns in this case. Inset of Fig. 2(a) shows a SEM scan of the measured sample. The cleaved area is marked.

In the C-CDW state, we observe a small, spatially uniform spectral weight at the Fermi level, originating from the tail of the flat band located at a binding energy of approximately 100 meV. In the hidden state, however, regions of high intensity indicate the metallic parts of the sample where the spectral gap is closed. The transition between the C-CDW and hidden states is fully reversible; in fact, the data in Fig. 2(a) was measured after the data in Fig. 2(b) by warming the sample and cooling it down again.

The use of a current pulse to drive the transition results in an inherently inhomogeneous state. Unlike a laser pulse, the current flow profile between the contacts cannot be precisely controlled and is generally non-uniform. Consequently, it is reasonable to assume that metallic regions form where the current density is sufficiently high. This inhomogeneity is not a characteristic of the hidden state but rather specific to the sample.

We observed different patterns of phase separation in the samples we measured and were unable to find defects on the sample surface that pin the metallic parts in the hidden state, suggesting that the switching is governed by the bulk current flow profile. Recently, it has been suggested that the metallic areas are more likely to form at the sample boundary [32].

In our study, we found an area of approximately 500 μm^2 that turned metallic, which is much larger than the typically reported domain size of $\sim 100 \text{ nm}^2$ in the hidden state [31]. Each pixel in Fig. 2 contains many such domains.

Next, we compare in detail the spectra in the C-CDW state and the metallic regions of the hidden state. In Fig. 3, we present typical microARPES data along the $\Gamma - M$ direction, measured using 80 eV photon energy and a sub-micron spot size. Fig. 3(a) shows the timeline of the experiment. First, the sample was cooled to 40 K. The data before any current pulse was applied is shown in Fig. 3(b), revealing the signature of C-CDW gaps and a flat band around the Γ point. A 140 mA, 1 ms long pulse was then applied, reducing the resistance by a factor of four. Fig. 3(c) presents the ARPES data after the current pulse, showing a suppression of the CDW gaps and a band crossing the Fermi level at $k_F = \pm 0.4\text{\AA}^{-1}$. The intensity at the Γ point is significantly suppressed. The sample was then removed from the cryo-manipulator and allowed to warm up in the vacuum chamber for roughly 10 minutes before being cooled back to base temperature. Following this thermal cycle, the resistance partially recovered to about half of the original value. It is important to note that the exact temperature during this warm-up sequence is unknown. The data in Fig. 3(d) shows developed C-CDW gaps and a partial recovery of the flat band. A second current pulse was then applied and the resistance dropped to a tenth of the original resistance. Fig. 3(e) shows ARPES data after the second current pulse. Again, the C-CDW gaps are closed and a metallic band is formed. For comparison, we show in white dashed-line the band-dispersion measured at room temperature, in the NC-CDW state, using a ~ 100 microns spot size. The agreement with the hidden state dispersion is remarkable.

In Fig. 3(f-h) we show energy distribution curves (EDCs) at $k=0$ (f), $k=0.32\text{\AA}^{-1}$ (g) and at $k_F=0.44\text{\AA}^{-1}$ (h) showing the flat band and the C-CDW gaps. At the Γ point (f) we can see a suppression of the flat band in the hidden state. This band is not fully recovered after the thermal cycle. The small peak at $\approx -0.45\text{eV}$ is a signature of the folded band due to the C-CDW and is absent in the hidden phase. In (g) we find well developed gaps in the EDCs that correspond to the C-CDW state (marked with gray dashed lines), and a suppression of the gap in the EDCs measured in the hidden state. In (h) we show a metallic Fermi-edge in the EDCs taken in the hidden state and a gap at the Fermi-level for EDCs in the C-CDW state.

ARPES intensity maps measured in the hidden state at two different locations on the sample, one in a metallic region and the other in a gapped region are shown in Fig. 4. In the metallic part, at the Fermi-level, we find a clear

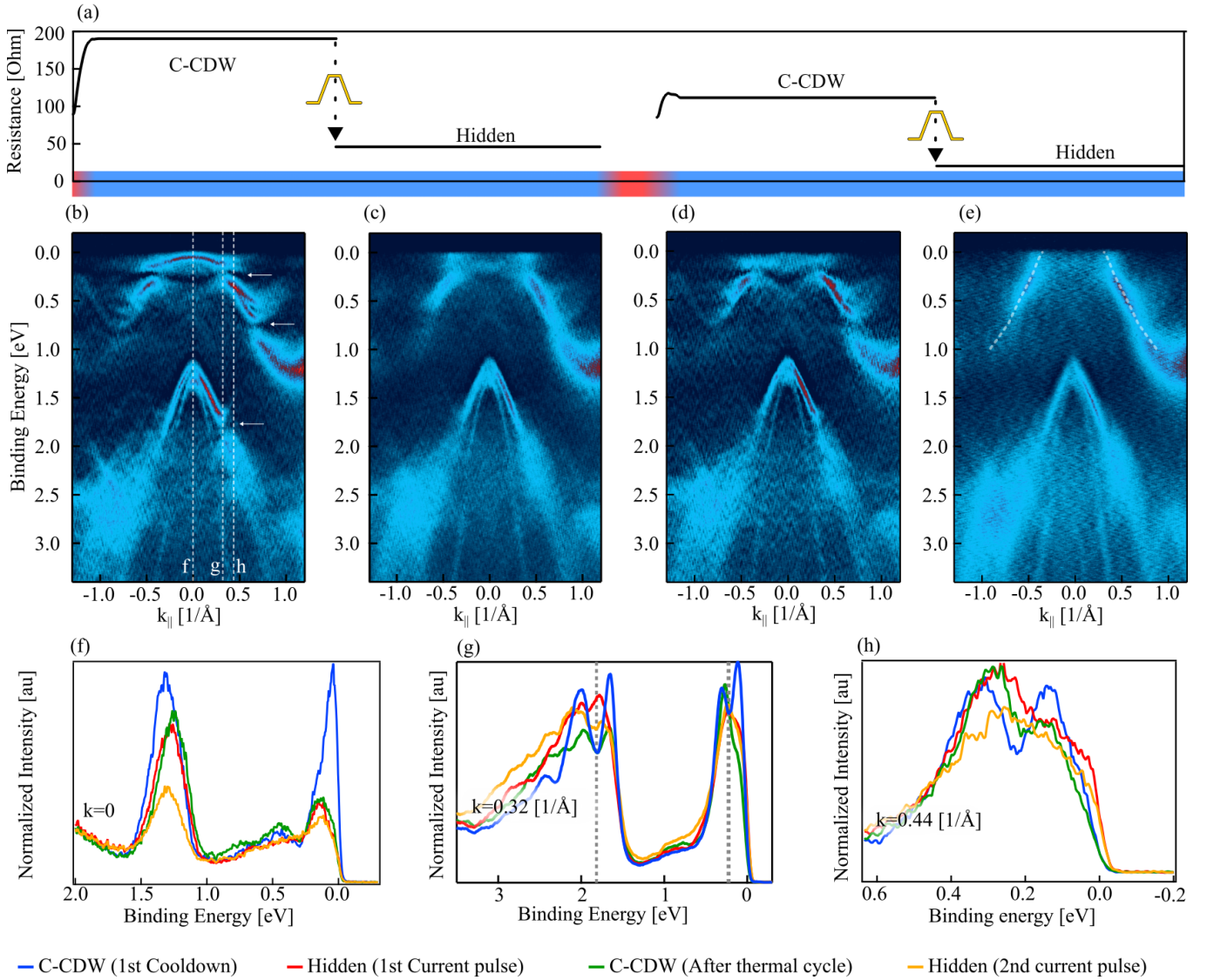


FIG. 3. ARPES spectra in the hidden state. microARPES spectra at 40K, measured with 80eV photons along the Γ -M direction. (a) the experimental timeline, showing the sample's resistance plotted as a function of time. (b) the ARPES image after the initial cool-down, in the C-CDW state. The resistance of the sample at this stage is $\sim 200\Omega$. One can see the characteristic flat-band at Γ and the CDW gaps marked by white arrows. The dashed white lines indicate the momenta at which the EDCs are displayed in panels (f)–(h). (c) the spectra after a 140mA, 1ms long current pulse, the resistance dropped to 46Ω . The CDW is highly suppressed, as evidenced by the suppressed band-folding and CDW gaps. The band is crossing the Fermi level at $k_{||} = 0.44\text{\AA}^{-1}$. (d) ARPES image after the sample was removed from the manipulator, allowed to warm up, and then reinserted and cooled down. The sample resistance is 115Ω , not fully restored. The CDW gaps are partially recovered. (e) ARPES image after a second, 140mA, pulse was applied. The resistance dropped to 20Ω . Again, the flat band and the CDW gaps vanish. The dashed white line shows the dispersion in the NC-CDW state measured at room temperature using standard ARPES. The measurements in (b-d) were all measured at roughly the same position on the sample. (f) EDCs at the Γ point. The flat band is suppressed by the pulses and only partially recovered in (c). The folded band due to the C-CDW is visible as a peak at -450meV in the C-CDW state (green, blue) while absent in the hidden state (red, orange). (g) EDCs at $k = 0.32\text{\AA}^{-1}$. Gray dotted lines show the C-CDW gaps position. The gap is clear in the C-CDW state (blue, green) and it is strongly suppressed in the hidden state (red, orange). (h) EDCs taken at $k_F = 0.44\text{\AA}^{-1}$ show a Fermi-edge for the EDCs measured in the hidden state (red, orange).

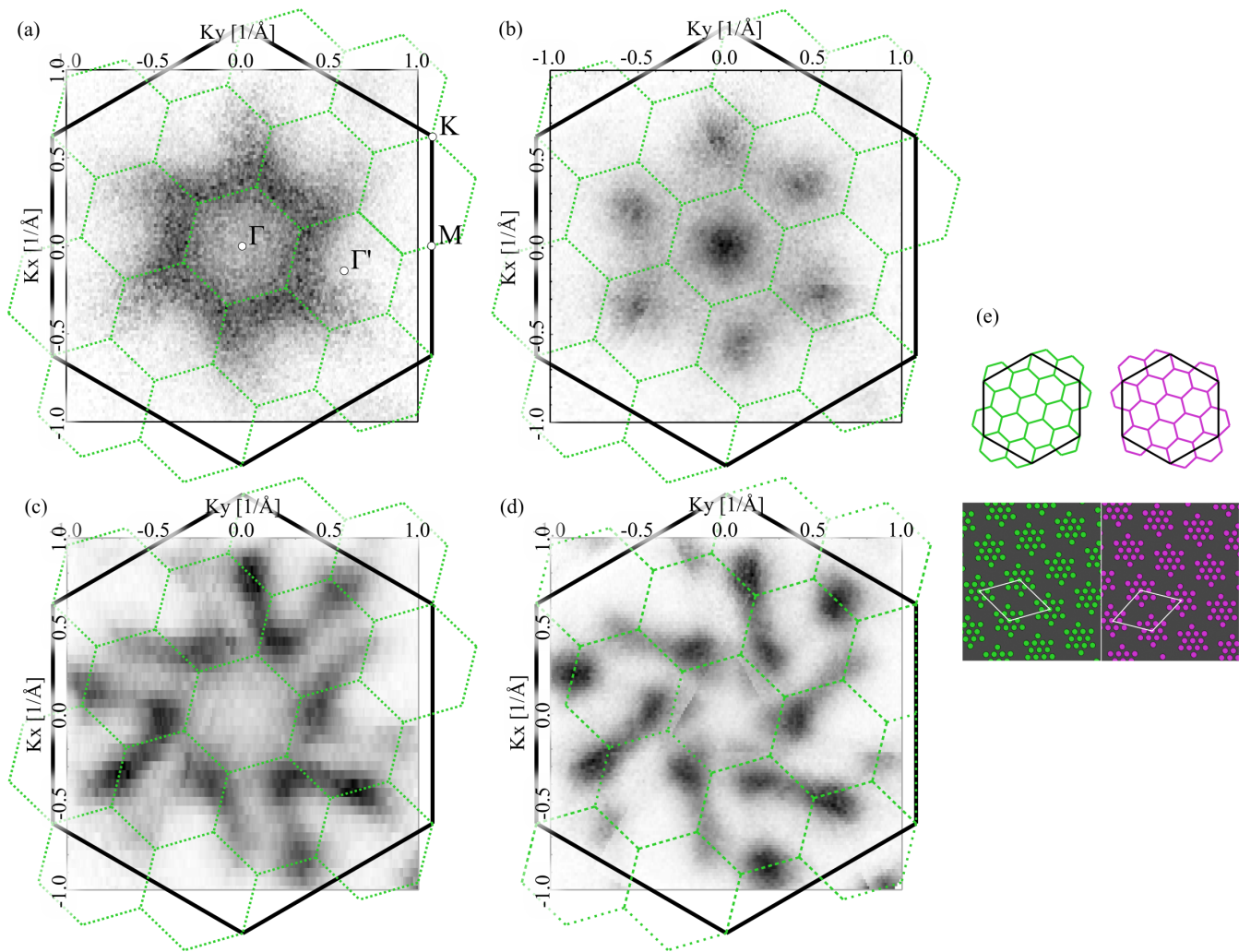


FIG. 4. **ARPES intensity maps.** Constant energy maps at metallic and gapped regions in the hidden state. Data measured at a 80eV photon energy. The maps are created by rotating the measured region by 120 degrees and stitching it together. The large hexagon in solid black line represents the normal state Brillouin zone (BZ). Small hexagons in green are the CDW reconstructed BZs. (a) Fermi surface from a metallic region averaging 10meV around the Fermi-level. (b) constant energy map from an insulating region, measured at a binding energy of 30 ± 5 meV. (c-d) Constant energy maps measured at $300 \text{meV} \pm 5 \text{meV}$ in the metallic and insulating parts, respectively. Both show a distinct chirality which originates from the formation of the star-of-David clusters. We find the same chirality in the metallic and insulating regions. (e) The two possible mirror-symmetry breaking C-CDW configurations. top: BZ of each configuration resulting from the real space C-CDW configuration illustrated below.

Fermi-surface (Fig. 4a). This FS is the origin of the enhanced conductivity in the hidden state. The FS is similar to the FS found in the high temperature NC-CDW state [33]. It consists of six elliptical pockets centered around the M-points. The Fermi pockets are gapped near the BZ edge because of the CDW, resulting in an incomplete Fermi surface [17, 34].

In the gapped regions, there is no Fermi surface, but we observe intensity at low binding energies extending almost to the Fermi level. Fig. 4(b) shows an intensity map at a binding energy of 30 meV. We find some spectral weight at the Γ point of the atomic Brillouin zone (solid black lines) and weaker replicas at the Γ points of the CDW-folded Brillouin zones (green dashed lines).

The electronic structure at higher binding energies indicates that a CDW deformation persists in the hidden state, even though the gaps are suppressed. In Fig. 4(c) and (d), we compare intensity maps at a binding energy of 300 meV in a metallic region (c) and a gapped region (d). Both datasets exhibit a chiral pattern attributed to mirror symmetry breaking caused by the formation of star-of-David clusters [21].

Throughout the text, we refer to the band structure of 1T-TaS₂ as chiral, in accordance with the accepted notation in the field. However, it is important to note that 1T-TaS₂ is centrosymmetric, and therefore not chiral in the

crystallographic sense. Instead, it is more accurately described as *pseudochiral*, a state characterized by the absence of mirror symmetry in the bulk 3D band structure [35].

The two possible ways to arrange the BZ in the C-CDW are shown in Fig. 4(e). Interestingly, we find that the emerging Fermi surface also breaks mirror symmetry (see supplementary material), seemingly inheriting its chirality from the CDW domains.

Furthermore, by comparing the chiral patterns at the same metallic point in both the hidden state and before the application of the current pulse, we demonstrate that the chirality remains unchanged by the current pulse. This data is presented in the supplementary material. This strongly suggests that transitioning into the hidden state does not involve a complete melting of the CDW. This finding aligns with the distinct chirality of the domains observed in real-space STM data [31].

The data from the metallic parts of the hidden state, including both the dispersion and the Fermi surface, closely resemble those of the NC-CDW state[36]. However, STM measurements reveal that in the hidden phase, the C-CDW is split into a disordered network of domains, each approximately tens of nanometers in size[31]. This domain configuration is distinct from that observed in the NC-CDW state.

The spot size used covers approximately 1000 domains. Given that the domain walls are around $\sim 1\text{\AA}$ in width[18], their contribution to the ARPES spectra is negligible. This, along with the distinct chirality of the Fermi surface, confirms that the metallic nature of the hidden state is not due to conducting domain walls.

After confirming that the CDW persists following the pulse current in both the metallic and gapped regions of the sample, we investigate the reasons for the differences between these regions. In Fig. 5, we present photon energy-dependent data measured at representative points in both regions. The out-of-plane dispersion was measured at a fixed parallel momentum, $k_{\parallel} = 0.66\text{\AA}^{-1}$, near the center of the reconstructed Brillouin zone, Γ' (as indicated by the dashed line in Fig. 5(a)).

Fig. 5(a and b) correspond to a gapped region. Fig. 5(a) shows data along Γ -M measured using 80eV photons and in (b) we show a color plot combining the EDCs at different k_z values. The k_z dispersion of the two uppermost sub-bands formed by the C-CDW, extracted by tracking the maxima in the EDCs, are shown in Fig. 5(e and f). The bandwidths of the two bands are 100 meV and 50 meV, respectively. Notably, both bands show a clear doubling of the expected periodicity, indicating a doubling of the unit cell. This observation is consistent with a $Q=0.5$ charge density wave (CDW) out-of-plane or a dimerization of pairs of star-of-David clusters on two neighboring planes.

When examining the k_z dispersion in the metallic regions, we observe a different behavior. In Figs. 5(c) and 5(d), we present data along Γ -M measured using 80eV photons and the photon energy dependence of the EDCs measured in a metallic part of the sample. The extracted dispersion is shown in Fig. 5(g), revealing only one band at this k_{\parallel} value. The bandwidth is approximately 200 meV, which is significantly larger than that observed in the insulating region. Notably, we do not find double periodicity; instead, the dispersion is in agreement with the atomic lattice unit cell.

This can explain the metallic behavior. In the C-CDW state, the doubling of the unit cell perpendicular to the planes results in two electrons per unit cell, causing the valence band to be fully occupied, as expected in a band insulator. The current pulse disrupts the dimerization out-of-plane but maintains the CDW deformation within the planes. Although the in-plane hopping compared to the on-site Coulomb interaction places the sample beyond the Mott limit, the significant out-of-plane dispersion is sufficient to restore the metallic behavior of the 3D sample.

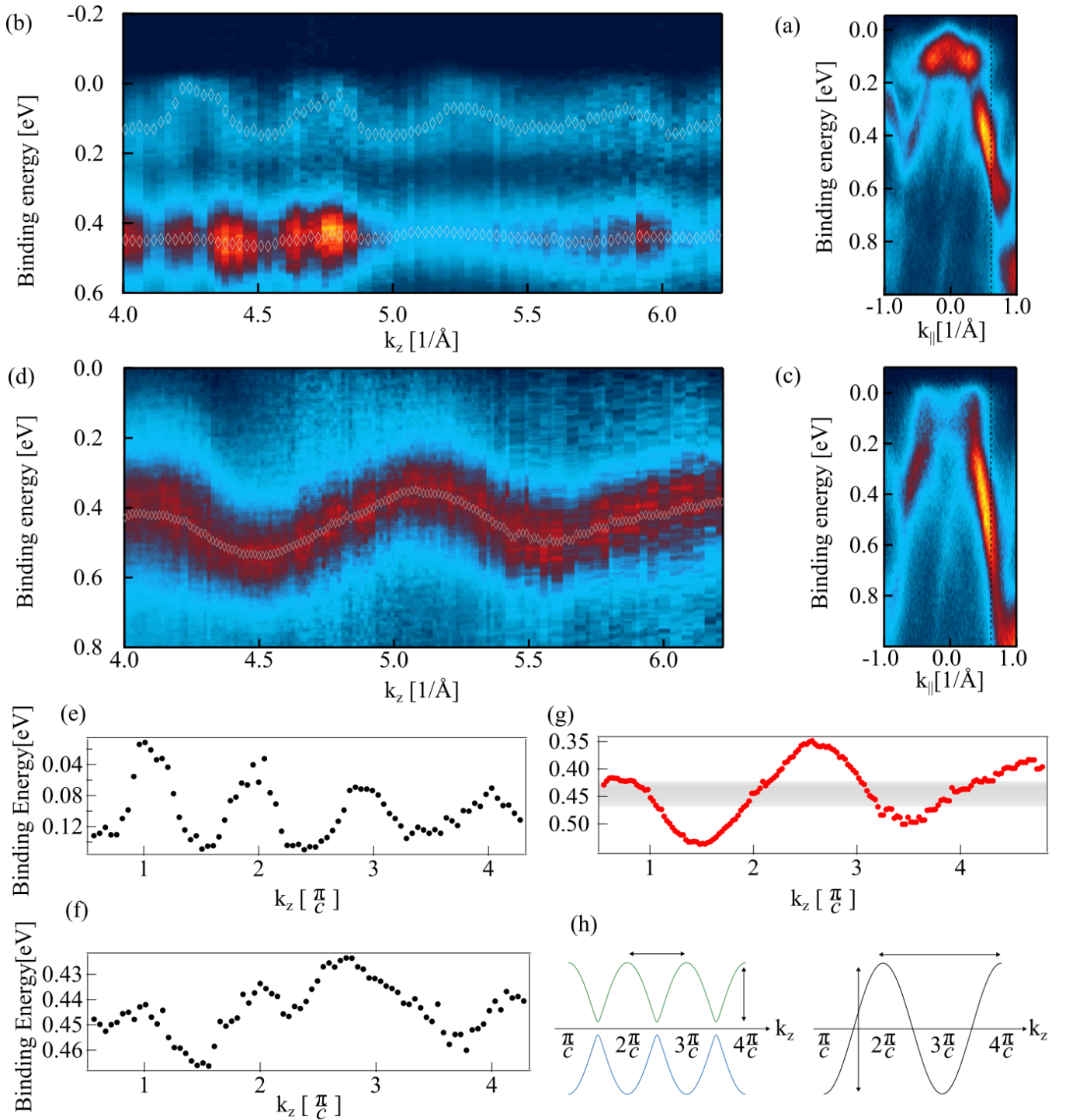


FIG. 5. **Out-of-plane dispersion.** (a) ARPES image along Γ -M from a gapped region in the hidden state measured with 80eV photons. Black dotted line marks k_{\parallel} where the photon energy scan was measured. (b) Intensity as a function of binding energy and k_z for photon energies between 48eV and 140eV. Gray diamonds mark the peak binding energy at each k_z . Each EDC is normalized by the intensity at the peak at low binding energies. The dispersion of the two bands exhibits a periodicity that is double the expected value based on the atomic unit cell size. (c) and (d) same as (a) and (b) measured in a metallic region. Gray diamonds mark the peak binding energy at each k_z . EDCs are normalized by the intensity at the maximum. Here, the dispersion periodicity follows the atomic BZ. (e) and (f) the k_z dispersion of the flat band and the second valence band, respectively, as extracted from panel (b). (g) the k_z dispersion of the top most valence band in the metallic region as extracted from (d). The shaded gray area represents the bandwidth in shown in (f). (h) Schematic illustration of the k_z dispersion. The right side shows the dispersion of a band with 1 electron per unit cell. The left side shows the dispersion when the unit cell is doubled, either due to dimerization or a 2-unit cell CDW.

III. SUMMARY

Our study reveals that the hidden state in 1T-TaS₂ exhibits a hole-like band crossing the Fermi level, resulting in a Fermi surface reminiscent of the NC-CDW phase. This similarity is not unexpected, given the structural resemblance between the two phases, both characterized by domains of commensurate CDW. However, the underlying mechanisms rendering these phases metallic remain elusive. While it was hypothesized that conducting domain walls, where the order parameter $\Delta = 0$, contribute to the conductivity by forming channels, our ARPES measurements of the hidden phase suggest a different scenario.

We demonstrate that the hidden Fermi surface displays distinct chirality, originating from the C-CDW arrangements—a property inherent to the domains rather than the domain walls. Additionally, ARPES, which is sensitive to the surface area, indicates that the contribution from domain walls is negligible. This observation implies that each domain is intrinsically metallic and possesses an in-plane C-CDW configuration, suggesting that additional factors influence the metallic behavior.

We propose that the metallic behavior originates from the out-of-plane electronic dispersion. The periodicity of the dispersion along k_{\perp} indicates a doubling of the Brillouin zone in the out-of-plane direction within the C-CDW state, consistent with the previously reported layer dimerization [29]. Upon transitioning to the hidden state, the out-of-plane dispersion changes, suggesting that star-of-David clusters on neighboring planes are no longer correlated. This leads to a profound change in the electronic structure: instead of having two electrons per unit cell in the C-CDW state, we now have a metallic half-filled band. The resulting band structure is unusual for a TMD, as it has a larger hopping constant normal to the Ta planes than within the planes.

IV. METHODS

A. Sample preparation

1T-TaS₂ single crystals were prepared as described in Ref. [37]. Samples of 1T-TaS₂ were prepared for nanoARPES experiments. Single crystals were cut into narrow bridges 200-500 μm in width. The samples were glued to a sapphire substrate and 4 contacts were made using Ag epoxy. The samples were cooled to 40K and cleaved under UHV conditions. The 4 contacts were used to drive a DC current pulse and to monitor the sample resistance. We emphasize that during the ARPES measurement no current was applied to the sample.

B. ARPES

Spatially resolved ARPES experiments were carried out in the I05 beamline at Diamond light source, UK. The spatial resolution is set by the beam spot-size, which in our experiment was either 500nm using a Zone-plate or 5 micrometers using a capillary mirror. Energy resolution was set to about 50meV. Data in the NC-CDW state was measured at the CASSIOPEE beamline at Soleil, France. Measurements were done at room temperature using 80eV photon energy. Beam spot size was 100 microns. Energy resolution was set to 20meV. The Fermi-level was determined by measuring a metallic sample at the same conditions.

C. calculation of k_{\perp}

We have used the three-step-model for the out-of-plane momentum $k_z = \sqrt{\frac{2m}{\hbar^2}(E_k \cos^2 \theta + V_0)}$ [38], where V_0 is the inner potential. We have used $V_0 \sim 15.4\text{eV}$, obtained by following the normal-crystal periodicity over 3 BZs, demanding $\Delta k_z^{\Gamma} = \frac{2\pi}{c}$ ($c = 5.861\text{\AA}$).

V. ACKNOWLEDGMENTS

We thank Assa Auerbach and Daniel Podolsky for useful discussions. We acknowledge Diamond Light Source for time on Beamline i05 under Proposal SI33131. We acknowledge SOLEIL for provision of synchrotron radiation facilities under proposal 20230771 and we would like to thank Chiara Bigi and Francois Bertran for assistance in

using beamline CASSIOPEE. The work at the Technion was supported by Israeli Science Foundation grant number ISF-1263/21.

-
- [1] F. Di Salvo, B. Bagley, J. Voorhoeve, and J. Waszczak, *Journal of Physics and Chemistry of Solids* **34**, 1357 (1973).
- [2] S. H. Sung, N. Schnitzer, S. Novakov, I. El Baggari, X. Luo, J. Gim, N. M. Vu, Z. Li, T. H. Brintlinger, Y. Liu, W. Lu, Y. Sun, P. B. Deotare, K. Sun, L. Zhao, L. F. Kourkoutis, J. T. Heron, and R. Hovden, *Nature Communications* **13**, 413 (2022).
- [3] M. Budden, T. Gebert, M. Buzzi, G. Jotzu, E. Wang, T. Matsuyama, G. Meier, Y. Laplace, D. Pontiroli, M. Riccò, F. Schlawin, D. Jaksch, and A. Cavalleri, *Nature Physics* **17**, 611 (2021).
- [4] J. Zhang, X. Tan, M. Liu, S. W. Teitelbaum, K. W. Post, F. Jin, K. A. Nelson, D. N. Basov, W. Wu, and R. D. Averitt, *Nature Materials* **15**, 956 (2016).
- [5] A. Zong, X. Shen, A. Kogar, L. Ye, C. Marks, D. Chowdhury, T. Rohwer, B. Freelon, S. Weathersby, R. Li, J. Yang, J. Checkelsky, X. Wang, and N. Gedik, *Science Advances* **4**, eaau5501 (2018).
- [6] A. De La Torre, D. M. Kennes, M. Claassen, S. Gerber, J. W. McIver, and M. A. Sentef, *Reviews of Modern Physics* **93**, 041002 (2021).
- [7] L. Stojchevska, I. Vaskivskiy, T. Mertelj, P. Kusar, D. Svetin, S. Brazovskii, and D. Mihailovic, *Science* **344**, 177 (2014).
- [8] L. Ma, C. Ye, Y. Yu, X. F. Lu, X. Niu, S. Kim, D. Feng, D. Tománek, Y.-W. Son, X. H. Chen, *et al.*, *Nature communications* **7**, 10956 (2016).
- [9] I. Vaskivskiy, I. A. Mihailovic, S. Brazovskii, J. Gospodaric, T. Mertelj, D. Svetin, P. Sutar, and D. Mihailovic, *Nature Communications* **7**, 11442 (2016).
- [10] R. Venturini, A. Mraz, I. Vaskivskiy, Y. Vaskivskiy, D. Svetin, T. Mertelj, L. Pavlovič, J. Cheng, G. Chen, P. Amarasinghe, *et al.*, *Applied Physics Letters* **120** (2022).
- [11] I. Vaskivskiy, J. Gospodaric, S. Brazovskii, D. Svetin, P. Sutar, E. Goreshnik, I. A. Mihailovic, T. Mertelj, and D. Mihailovic, *Science Advances* **1**, e1500168 (2015).
- [12] J. Maklar, J. Sarkar, S. Dong, Y. A. Gerasimenko, T. Pincelli, S. Beaulieu, P. S. Kirchmann, J. A. Sobota, S. Yang, D. Leuenberger, R. G. Moore, Z.-X. Shen, M. Wolf, D. Mihailovic, R. Ernstorfer, and L. Rettig, *Science Advances* **9**, eadi4661 (2023), <https://www.science.org/doi/pdf/10.1126/sciadv.adi4661>.
- [13] I. Vaskivskiy, A. Mraz, R. Venturini, G. Jecl, Y. Vaskivskiy, R. Mincigrucchi, L. Foglia, D. De Angelis, J.-S. Pelli-Cresi, E. Paltanin, *et al.*, *Nature Photonics* , 1 (2024).
- [14] D. Mihailovic, D. Svetin, I. Vaskivskiy, R. Venturini, B. Lipovšek, and A. Mraz, *Applied Physics Letters* **119** (2021).
- [15] A. Mraz, R. Venturini, D. Svetin, V. Sever, I. A. Mihailovic, I. Vaskivskiy, B. Ambrozic, G. Dražič, M. D'Antuono, D. Stornaiuolo, *et al.*, *Nano Letters* **22**, 4814 (2022).
- [16] S. C. Bayliss, A. M. Ghorayeb, and D. R. P. Guy, *Journal of Physics C: Solid State Physics* **17**, L533 (1984).
- [17] K. Rossnagel, *Journal of Physics: Condensed Matter* **23**, 213001 (2011).
- [18] X. L. Wu and C. M. Lieber, *Science* **243**, 1703 (1989).
- [19] R. E. Thomson, B. Burk, A. Zettl, and J. Clarke, *Physical Review B* **49**, 16899 (1994).
- [20] X. L. Wu and C. M. Lieber, *Physical Review Letters* **64**, 1150 (1990).
- [21] H. Yang, K. He, J. Koo, S. Shen, S. Zhang, G. Liu, Y. Liu, C. Chen, A. Liang, K. Huang, M. Wang, J. Gao, X. Luo, L. Yang, J. Liu, Y. Sun, S. Yan, B. Yan, Y. Chen, X. Xi, and Z. Liu, *Physical Review Letters* **129**, 156401 (2022).
- [22] G. Liu, T. Qiu, K. He, Y. Liu, D. Lin, Z. Ma, Z. Huang, W. Tang, J. Xu, K. Watanabe, *et al.*, *Nature nanotechnology* **18**, 854 (2023).
- [23] E. Tosatti and P. Fazekas, *Le Journal de Physique Colloques* **37**, C4 (1976).
- [24] K. T. Law and P. A. Lee, *Proceedings of the National Academy of Sciences* **114**, 6996 (2017).
- [25] Z. Wu, K. Bu, W. Zhang, Y. Fei, Y. Zheng, J. Gao, X. Luo, Z. Liu, Y.-P. Sun, and Y. Yin, *Phys. Rev. B* **105**, 035109 (2022).
- [26] P. Fazekas and E. Tosatti, *Physica B+C* **99**, 183 (1980).
- [27] C. J. Butler, M. Yoshida, T. Hanaguri, and Y. Iwasa, *Nature Communications* **11**, 2477 (2020).
- [28] S.-H. Lee, J. S. Goh, and D. Cho, *Physical review letters* **122**, 106404 (2019).
- [29] Q. Stahl, M. Kusch, F. Heinsch, G. Garbarino, N. Kretzschmar, K. Hanff, K. Rossnagel, J. Geck, and T. Ritschel, *Nature Communications* **11**, 1247 (2020).
- [30] T. Ritschel, H. Berger, and J. Geck, *Phys. Rev. B* **98**, 195134 (2018).
- [31] Y. A. Gerasimenko, P. Karpov, I. Vaskivskiy, S. Brazovskii, and D. Mihailovic, *npj Quantum Materials* **4**, 1 (2019).
- [32] T. Devidas, J. T. Reichenadter, S. C. Haley, M. Sterenberg, J. E. Moore, J. B. Neaton, J. G. Analytis, B. Kalisky, and E. Maniv, *arXiv preprint arXiv:2405.02036* (2024).
- [33] T. Pillo, J. Hayoz, H. Berger, M. Grioni, L. Schlappbach, and P. Aebi, *Physical review letters* **83**, 3494 (1999).
- [34] C. Söhr, A. Stange, M. Bauer, and K. Rossnagel, *Faraday Discussions* **171**, 243 (2014).
- [35] A. Louat, M. D. Watson, T. K. Kim, D. Ni, R. J. Cava, and C. Cacho, *Communications Physics* **7**, 43 (2024).
- [36] E. Lahoud, O. N. Meetei, K. Chaska, A. Kanigel, and N. Trivedi, *Physical review letters* **112**, 206402 (2014).
- [37] A. Ribak, I. Silber, C. Baines, K. Chashka, Z. Salman, Y. Dagan, and A. Kanigel, *Phys. Rev. B* **96**, 195131 (2017).
- [38] A. Damascelli, *Physica Scripta* **2004**, 61 (2004).

VI. SUPPLEMENTARY MATERIALS

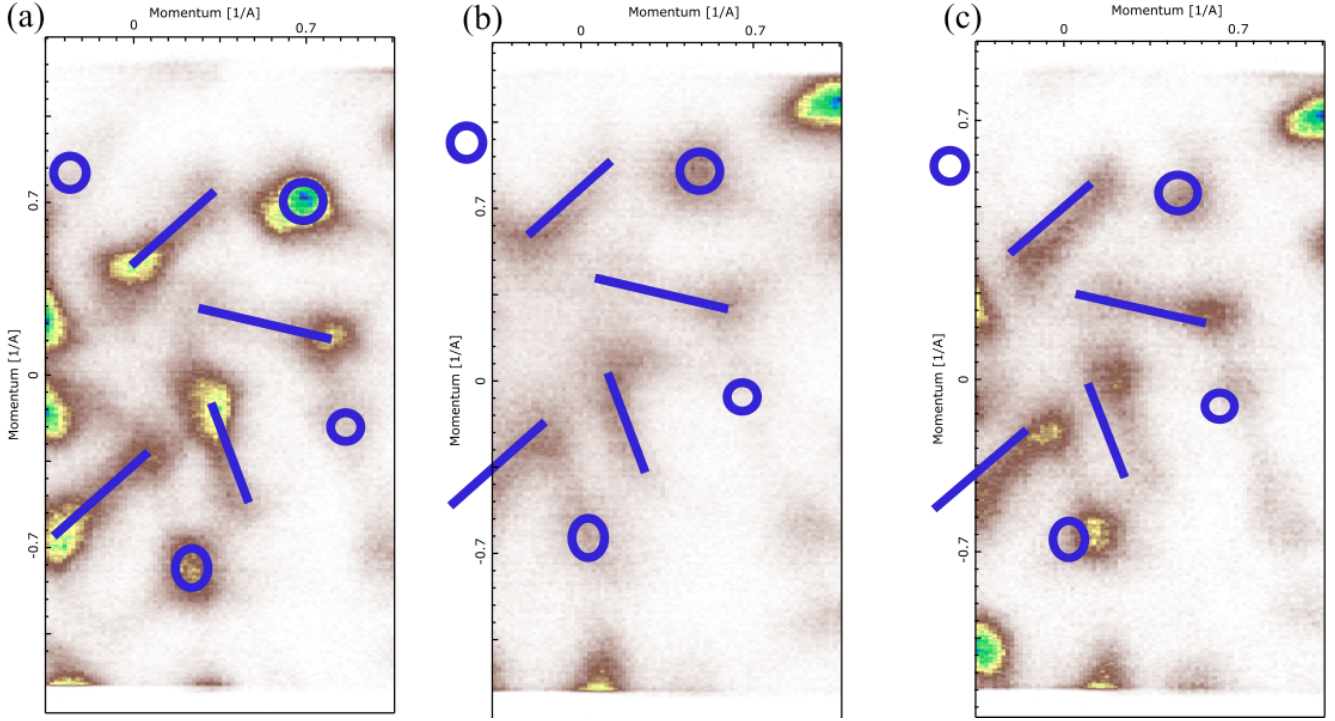


FIG. 6. **Polar maps at the same location.** ARPES polar maps measured with 72eV photon energy, at $E_b = 300\text{meV}$ (a) after initial cooldown (b) after pulse (c) after heating and cooling again (roughly the same location).

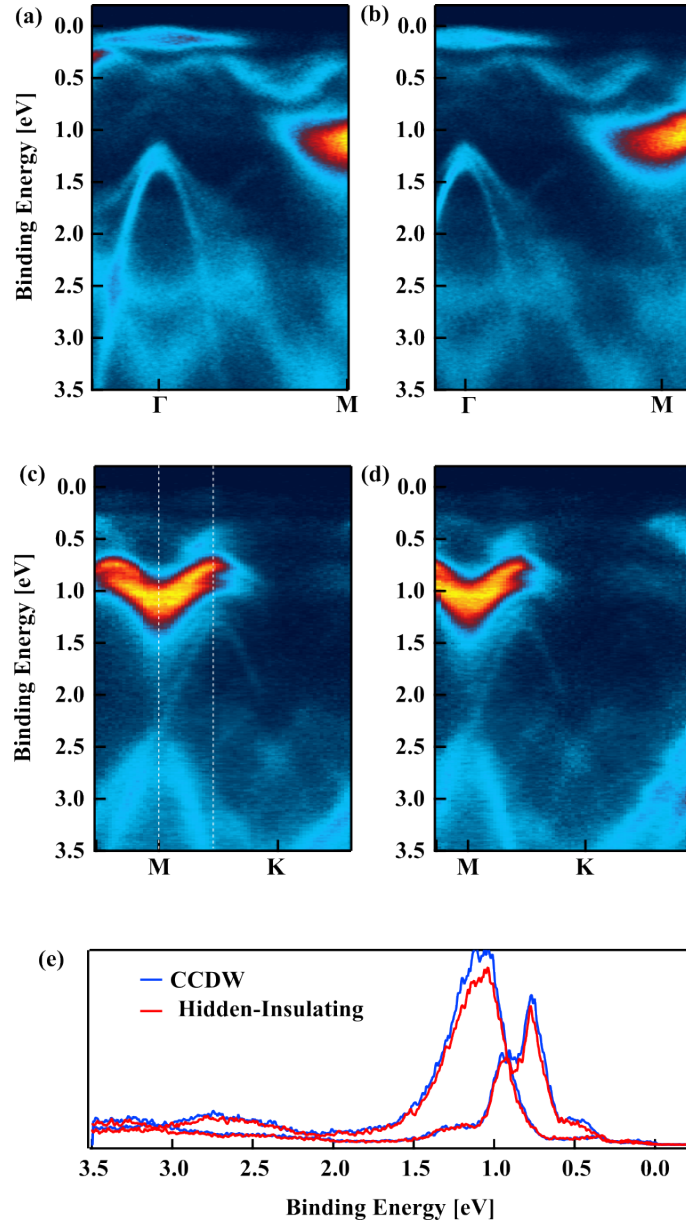


FIG. 7. Comparing the spectrum in the C-CDW state and in the insulating parts in the hidden state (a-b) ARPES images along the Γ -M direction for the C-CDW state and the insulating part of the hidden state, respectively. (c-d) ARPES images along the M-K direction for the C-CDW state and the insulating part of the hidden state, respectively. (e) EDCs at the momenta indicated by the dotted lines in (c), for both the C-CDW state and the insulating part of the hidden state.

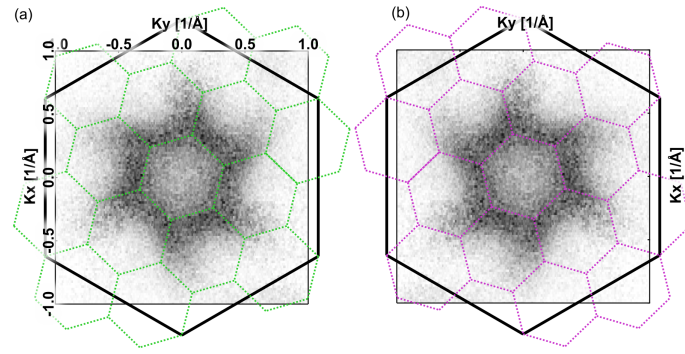


FIG. 8. **Hidden state Fermi-surface chirality** (a) FS of the hidden state, as shown in 4 (b) same as a but horizontally mirrored